# Absolute OH concentration profiles measurements in high pressure counterflow flames by coupling LIF, PLIF, and absorption techniques

**A. Matynia · M. Idir · J. Molet · C. Roche · S. de Persis · L. Pillier**

**Abstract** A high-pressure combustion chamber enclosing counterflow burners was set-up at ICARE-CNRS laboratory. It allows the stabilization of flat twin premixed flames at atmospheric and high pressure. In this study, lean and stoichiometric methane/air counterflow premixed flames were studied at various pressures (0.1 MPa to 0.7 MPa). Relative OH concentration profiles were measured by Laser Induced Fluorescence. Great care was attached to the determination of the fluorescence signal by taking into account the line broadening and deexcitation by quenching which both arise at high pressure. Subsequently, OH profiles were calibrated in concentration by laser absorption technique associated with planar laser induced fluorescence. Results are successfully compared with literature. The good quality of the results attests of the experimental set-up ability to allow the study of flame structure at high pressure.

## 1 Introduction

Combustion kinetics studies are necessary to understand the chemical phenomena occurring during combustion processes, and more largely, to determine the adequate conditions for a cleaner energy production. Actually, most practical combustion devices such as gas turbines and engines operate at high pressure and it is known that pressure greatly influences the combustion chemistry. Consequently,

A. Matynia · M. Idir · J. Molet · C. Roche · S. de Persis ·
L. Pillier (✉)
ICARE—Institut de Combustion, Aérothermique, Réactivité,
Environnement, UPR CNRS 3021, 1C, Avenue de la Recherche
Scientifique, 45071 Orléans Cedex 2, France
e-mail: pillier@cnrs-orleans.fr
Fax: +33-238-696004
url: http://www.cnrs-orleans.fr/icare/

the need of experimental data obtained at high pressure becomes more and more important. These high pressure experimental data are fundamental to develop and validate new kinetic combustion mechanisms.

In the laboratory, laminar flame structure study is a powerful tool for the analysis and the development of kinetic combustion mechanisms. However, such studies (for instance, among the large literature available, those reported in [1, 2]) are generally carried out on circular flat flame burner at subatmospheric and atmospheric pressures. Indeed, at high pressure, the flame front sits extremely close to the burner and it becomes impossible to obtain experimental profiles of temperature and species concentration through the flame front. Furthermore, the important reduction of the flame front thickness when pressure increases almost prevents the utilization of intrusive techniques such as probe sampling, and it becomes necessary to resort to nonintrusive optical diagnostics. Counterflow burners constitute an ideal configuration to overcome those problems. This alternative configuration allows the drifting of the flames away from the burner while keeping a 1D structure along the symmetrical axis of the burner. Moreover, this experimental device permits to obtain nearly adiabatic flames as those are stabilized far from the burner nozzles.

Among the existing diagnostic techniques in combustion applications, Laser Induced Fluorescence (LIF) appears as one of the most widely used [3]. It is mainly applied for the detection and measurement of species like OH, CH, NO, etc. Its success is principally due to its high sensitivity, its selectivity, and to the possibility to perform 2D measurements [4, 5]. Under high pressure environments, LIF can be used according to different excitation/detection schemes [6]. It can be employed in the linear [7–12], the saturated [13–15], and predissociated [16, 17] regimes. However, high pressure LIF measurements get greatly complicated by collision-

induced phenomena, such as absorption line-shape broadening and/or collisional de-excitation (quenching), and absorption/trapping phenomena. Depending on the experimental conditions, it is necessary to take into account those effects in the analysis of the LIF measured signals for the determination of either the relative or the absolute concentration. So, when measuring spatial LIF profiles, it is important to quantify the influence of those parameters according to pressure as well as their evolution through the flame.

A new facility composed of a high pressure combustion chamber has been developed at ICARE laboratory. The aim is to provide a new experimental device able to measure structure of high pressure flames with different kinds of laser and spectroscopic diagnostic techniques. In order to validate the installation, we first choose to make LIF measurements on the OH radical in laminar counterflow premixed $CH_4$/air flames at atmospheric and elevated pressures (up to 0.7 MPa). OH is selected because of its major role as intermediate species in hydrocarbon combustion processes. Moreover, its spectroscopy is well established. It is relatively abundant in methane/air flames ($>1000$ ppm), and it can be easily detected. Therefore, for the last decades, OH has been the subject of numerous studies, both for the determination of its concentration and for quantification of the different parameters that contribute to its LIF measurements [4, 5]. Only few studies of LIF measurements of OH in counterflow flames have been done so far [18–20] and those ones are limited to low or atmospheric pressures. So, the present work is in the line of bringing complementary data to the existing ones, especially at high pressure. In our approach, all the phenomena participating to the experimental LIF measured signals of OH are, as much as possible, taken into account.

## 2 Laser induced fluorescence

### 2.1 LIF signal in linear regime

Let us consider a pulsed laser beam at a wavelength $\lambda$ (or frequency $\nu$) tuned according to a given transition between a lower rotational level $J''$ and an upper one $J'$ of the $A^2\Sigma^+ - X^2\Pi$ ($\upsilon' = 1, \upsilon'' = 0$) vibrational band of OH (the $A - X$ $(1, 0)$ band is chosen here as it allows to minimize laser beam absorption phenomena). When this laser beam is focused at the center of a flame, the induced fluorescence is emitted according to different wavelengths. This emission is considered isotropic. In the linear regime of LIF, if a broadband detection scheme including both the $A^2\Sigma^+ - X^2\Pi$ $(0, 0)$ and $(1, 1)$ bands are considered, the relationship between the fluorescence signal $S_f$ detected and the OH density population $N_{OH}$ can be expressed as follows:

$$S_f = K_f^{coll} \cdot \xi_{abs}^\nu (\phi_L(\nu), \phi_{OH}(\nu)) \\ \cdot \eta_f \cdot F_B(J'', \upsilon'', T) \cdot N_{OH} \quad (1)$$

where:

- $K_f^{coll} = \frac{G \cdot \Omega \cdot V}{4\pi} \cdot h\nu_f$ is the experimental collection parameter with:

  $G$ the gain of the optical collection system,
  $\Omega$ the solid angle of collection in sr,
  $V$ the probe volume in $m^3$,
  $h$ the Planck's constant ($h = 6.625 \times 10^{-34}$ J s)
  $\nu_f$ the central frequency of the emitted fluorescence in $s^{-1}$ (considered constant whatever the flame conditions).

- $\xi_{abs}^\nu(\phi_L(\nu), \phi_{OH}(\nu)) = B_{J''J'} \cdot \int U_L(\nu) \cdot \phi_{OH}(\nu) \cdot d\nu$ reveals the efficiency of the laser photons to interact with the species according to the probed transition with:

  $B_{J''J'}$ the absorption Einstein coefficient in $J^{-1} m^3 s^{-2}$,
  $U_L(\nu)$ the local laser spectral energy density in $J m^{-3}$ s,
  $\phi_L(\nu)$ the spectral laser line shape in s,
  $\phi_{OH}(\nu)$ the absorption line shape in s.

  The term $U_L(\nu)$ can be expressed as

  $$U_L(\nu) = U_L \cdot \phi_L(\nu) \quad (2)$$

  where $U_L$ is the laser energy density in $J m^{-3}$.
  The expression of the integral then becomes

  $$\int U_L(\nu) \cdot \phi_{OH}(\nu) \cdot d\nu \\ = U_L \cdot \int \phi_L(\nu) \cdot \phi_{OH}(\nu) \cdot d\nu \quad (3)$$

  The integral $\int \phi_L(\nu) \cdot \phi_{OH}(\nu) \cdot d\nu$ corresponds to the spectral overlap function of the laser line with the absorption line shape.

- $\eta_f = \frac{\sum (A_{J'J''})_{obs}}{A_{eff} + Q_{eff}}$ is the fluorescence quantum yield that represents the ability of a molecule to emit fluorescence (i.e., spontaneous emission with rates $A_{J'J''}$) in the experimental observation spectral window compared to the overall deexcitation (radiative and nonradiative) processes. In a multilevel system, those deexcitation processes are characterized by an effective spontaneous emission coefficient $A_{eff}$ and by an effective quenching rate $Q_{eff}$. According to this definition of the quantum yield, collisional population redistribution in the excited level such as Rotational Energy Transfers (RET) and Vibrational Energy Transfers (VET) are taken into account. However, the calculations of $A_{eff}$ and $Q_{eff}$ are very complex due to the RET and VET and are strongly dependant on the collision rates of OH with neighboring atoms and molecules.

- $F_B$ is the Boltzmann fraction of the laser pumped rotational level $(J'', \upsilon'')$ at the temperature $T$ in K.

## 2.2 Analysis of the LIF signal

According to Eqs. (1) and (3), the fluorescence signal $S_f$ is equal to

$$S_f = N_{OH} \cdot K_f^{coll} \cdot B_{J''J'} \cdot U_L \cdot \left( \int \phi_L(\nu) \cdot \phi_{OH}(\nu) \cdot d\nu \right) \\ \cdot \eta_f \cdot F_B(J'', \upsilon'', T) \tag{4}$$

As soon as the laser energy density $U_L$ is proportional to the laser energy $E_L$ delivered per pulse, the instantaneous experimental measurements of the fluorescence signal $S_f$ and of $E_L$ lead to a simple relation of proportionality with $N_{OH}$ following the equation:

$$\frac{S_f}{E_L} \propto N_{OH} \cdot \left[ \left( \int \phi_L(\nu) \cdot \phi_{OH}(\nu) \cdot d\nu \right) \\ \cdot \eta_f \cdot F_B(J'', \upsilon'', T) \right] \tag{5}$$

Taking into account that $K_f^{coll}$ is a constant.

Such a formulation of the fluorescence signal permits to take into account the pulse to pulse energy fluctuations of the laser and gives a direct and simple relation with $N_{OH}$. One can say that the ratio $S_f/E_L$ is proportional to the product of an overall parameter (named in the following OP) and $N_{OH}$. OP corresponds to the terms between brackets in Eq. (5): the spectral overlap $\int \phi_L(\nu) \cdot \phi_{OH}(\nu) \cdot d\nu$, the quantum yield $\eta_f$, and the Boltzmann fraction $F_B(J'', \upsilon'', T)$.

The aim of the present section is to evaluate the influence of the variation of the overall parameter OP on the fluorescence signal. For that purpose, a numerical approach has been adopted in this work, where the chemical composition of the flame and the temperature profile are obtained with the help of the OPPDIF code [21] and the GRI-Mech 3.0 mechanism [22], considering adiabatic flames. Based on the expression of formula (5), the product of $N_{OH}$ and OP gives a picture of the evolution of the measured $S_f/E_L$.

Two scenarios are then possible. Either the relative profile of both $N_{OH}$ and $N_{OH}$ multiplied by the global parameter OP are identical or not.

Considering the first case, this means that the global influence of line broadening, quenching, VET and RET and Boltzmann fraction variation is kept constant through the flame. Then a one-point calibration measurement is sufficient to determine the absolute concentration profile along the whole flame axis.

In the second case, it is necessary to identify which parameter is preeminent among the others, and consequently, which physical effect is at the origin of this gap. Then a special attention should be paid on the accuracy and on the confidence level that can be given to the calculation of those parameters. Nevertheless, it must be kept in mind that such calculations are complex and can be affected by an important uncertainty. The calculation of those parameters is presented below.

### 2.2.1 Spectral overlap calculation

The spectral overlap $\int \phi_L(\nu) \cdot \phi_{OH}(\nu) \cdot d\nu$ represents the efficiency of the laser pumping on the targeted OH absorption line. It varies according to the intensity of the spectral covering of the OH line by the laser line. Assuming that the laser line shape does not change whatever the flame conditions, it is thus important to quantify the line broadening of the absorption transition.

In flame conditions, line broadening is the result of the contributions of homogeneous (i.e., collisional) and nonhomogeneous (i.e., Doppler) broadenings. In this work, the collisional broadening was calculated according to the methods developed by Rea et al. [23] (spectroscopic data from [23, 24]) and Bresson [25] (spectroscopic data provided in the thesis report). Bresson built his method based on the Rea et al. one and completed it by adding the dependence to the rotational levels. The resulting line shape is a Voigt profile, consisting in the convolution product of a Lorentzian profile, due to collisional broadening, with a Gaussian one, due to Doppler broadening. Assuming a Gaussian line shape for the laser line with a full width at half maximum of 0.1 cm$^{-1}$ and a Voigt profile for the absorbing transition, the spectral overlap was determined by calculating the integral of the product of those two line shapes (their areas are normalized to unity). For practical convenience and in order to compare our results with the ones from the literature [7], the spectral overlap is expressed in cm. The collisional line broadening was calculated for the $P_1(7)$ line of the $A^2\Sigma^+ - X^2\Pi$ ($\upsilon' = 1$, $\upsilon'' = 0$) band of OH in the burned gases of a $CH_4$/air flame close to stoichiometry, at different pressures. For that purpose, the burned gases are considered to be a mixture of 72 % $N_2$, 19 % $H_2O$, and 9 % $CO_2$. Unfortunately, no data concerning the collisional broadening parameters of OH with $O_2$ were available in the literature. Collisional broadening obtained through Bresson and Rea et al. methods are quite similar in the temperature domain where OH is present, i.e., between 800 K and 2000 K. Thus, as the Rea et al. method is used with more recent spectroscopic data, and as to our knowledge, the Bresson method has not been published in literature; in the following works, we will consider the Rea et al. method. The calculated spectral overlap is presented in Fig. 1.

The results show that, as the pressure increases, the OH absorption line broadens due to collision effects, and consequently, the overall excitation efficiency, i.e., the spectral overlap, decreases. When the temperature increases, the Doppler broadening increases and the collisional broadening decreases (as density decreases). Thus, at atmospheric pressure, the Doppler broadening dominates above around 800 K. As a consequence, OH absorption line broadens above 800 K and the spectral overlap decreases. However, at higher pressure, the collisional broadening dominates so
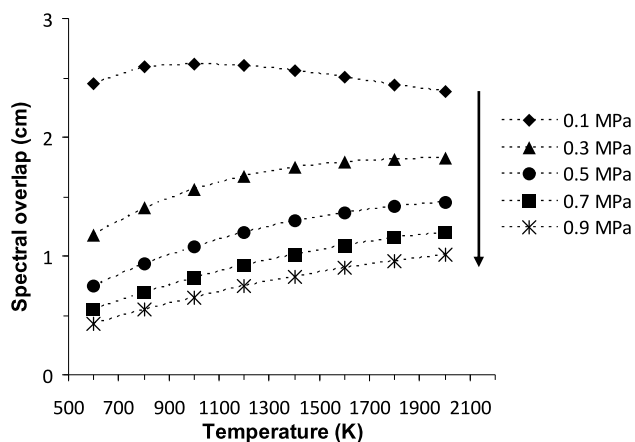
**Fig. 1** Spectral overlap (in cm) of a Gaussian laser line of 0.1 cm$^{-1}$ FWHM with the P$_1$(7) line of OH $A - X$ (1, 0) band as a function of the temperature (in K), for different pressures in the range 0.1–0.9 MPa

that, when the temperature increases, OH absorption line becomes thinner and the spectral overlap increases. Those results are in accordance with [7].

### 2.2.2 Fluorescence quantum efficiency evaluation

The quantification of the fluorescence quantum yield $\eta_f$ implies the determination of $A_{\text{eff}}$ and $Q_{\text{eff}}$ coefficients. However, this calculation is very complicated notably because it requires an accurate knowledge of VET and RET. The latter cannot be determined without the help of sophisticated models such as the LASKIN code [26].

In our case, a wide band detection scheme, including the overall radiation emitted from the $A - X$ (0, 0) and (1, 1) bands, has been employed to collect the fluorescence. By using this scheme, the emitted fluorescence becomes insensitive to the relative influence of the VET and RET [3]. Consequently, in our case, a simplified two level system is considered and the effective spontaneous emission coefficient $A_{\text{eff}}$ and the effective quenching rate $Q_{\text{eff}}$ are replaced by $A_{J'J''}$ and $Q_{J'J''}$, where the subscript $J''$ represents the fundamental level and the subscript $J'$ represents the excited level. Considering this simplified approach, the de-excitation collision rate $Q_{J'J''}$ (s$^{-1}$) can be expressed as follows:

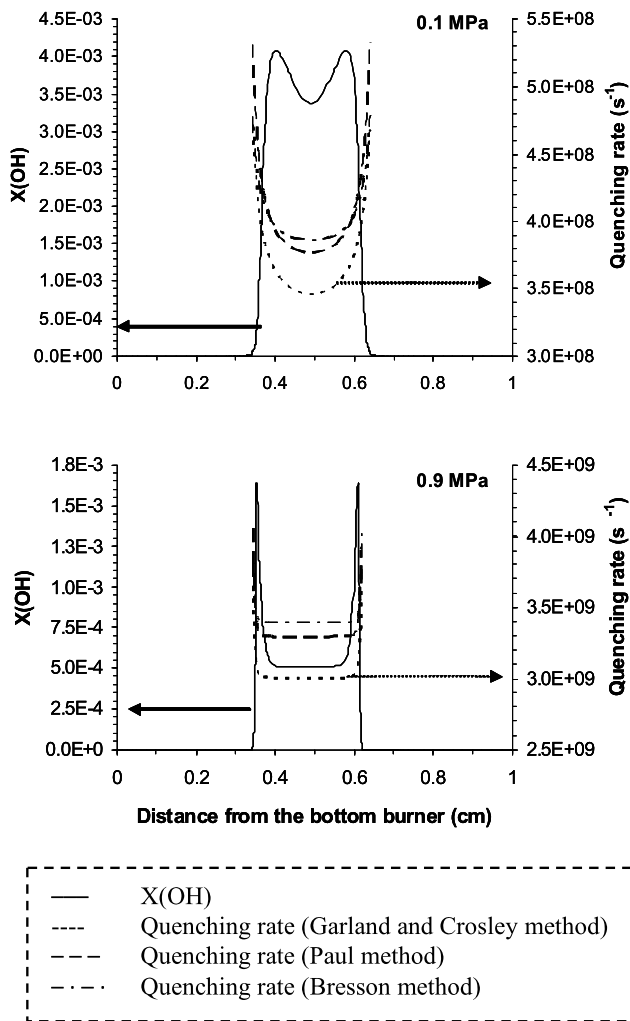$$Q_{J'J''} = N_{\text{tot}} \cdot \sum_i \chi_i \sigma_i v_i \tag{6}$$

where $i$ is summed among all the collision partners, $\chi_i$ is the corresponding molar fraction, $\sigma_i$ is the quenching cross section (m$^2$), $v_i$ the average relative velocity between OH and the collision partner $i$ (m s$^{-1}$), and $N_{\text{tot}}$ is the total density population (molecules m$^{-3}$). For flames at pressures higher than 0.1 MPa, the OH quenching rate is high and cannot be experimentally measured with a conventional nanosecond pulsed laser [27, 28]. Hence, in our case, the only approach to quantify the quenching rate at high pressure is

through calculations, taking into account quenching cross sections available in the literature as well as concentrations of major colliders obtained experimentally or by simulation. In the present work, we calculated the quenching rate by considering that the major colliding species are: CH$_4$, O$_2$, H$_2$, CO, H$_2$O, and CO$_2$. Spatial profiles of temperature and concentration of those species along the centerline of the counterflow flames were calculated with the OP-PDIF code [21] and the GRI-Mech 3.0 mechanism [22] in the case of adiabatic flames. The corresponding quenching cross sections were simulated as a function of the temperature, based on the models of Garland and Crosley [29], Paul [30] and Bresson [25]. Those models rely on two theoretical bases: the "collisional complex model," proposed by Garland and Crosley [29] and the "harpooned model," proposed by Paul [30]. The Bresson model is based on the "harpooned model" of Paul and completes it by adding dependence to the rotational levels.

Figure 2 presents the spatial profiles of the quenching rates calculated according to those three models for the lean CH$_4$/air flame (equivalence ratio E.R. = 0.7) at 0.1 and 0.9 MPa. The simulated spatial OH molar fraction profile is also plotted in Fig. 2 in order to correlate it with the spatial variations of the quenching rate across the flame. Calculated values of quenching rates are of the same order according to the three methods employed (differences around 10 % at both pressures). As it could be expected, highest differences are observed between the Garland and Crosley model [29] and the Paul [30] and Bresson models [25] which are based on two different theoretical models.

Calculated values at 0.1 MPa are of the same order than experimental values available in the literature, which is noteworthy with regards to the assumptions made for the quenching calculation. Indeed, calculated values with the Garland and Crosley, Paul and Bresson models are $3.46 \times 10^8$ s$^{-1}$, $3.77 \times 10^8$ s$^{-1}$, and $3.87 \times 10^8$ s$^{-1}$, respectively, while experimental values measured by Schwarzwald et al. [27] (for a CH$_4$/air flame with an equivalence ratio ranging from 0.77 to 1.43) and Tsujishita and Hirano [28] (for a CH$_4$/air flame with an equivalence ratio of 1.19 and 1.59) are $5.15 \times 10^8$ s$^{-1}$ and $5.6 \times 10^8$ s$^{-1}$, respectively (values averaged over the equivalence ratio range).

It can be observed that the quenching rate varies mainly in the OH concentration gradients corresponding to the flame fronts where temperature and flame composition vary significantly. Considering the domain of increasing gradients of OH concentration from 1 % to 100 % of its maximum value, those variations reach around 30 % at 0.1 MPa and 20 % at 0.9 MPa for the three models. Those variations are much weaker in the burned gases, defined here as the area between the maximum values of OH, and are below 5 % at 0.1 MPa and 3 % at 0.9 MPa, for the three models. This feature is explained by the fact that temperature and gas composition are nearly constant in this area.
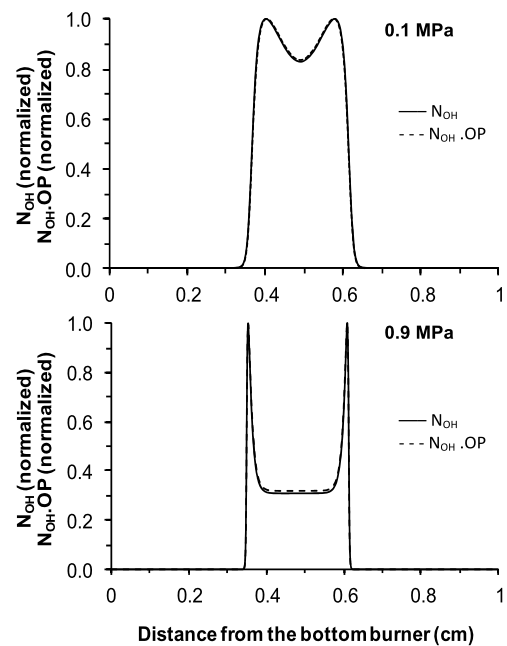
Fig. 3 Comparison between the normalized $N_{OH}$ profile with the product (normalized $N_{OH} \times$ OP*) profile for the lean (E.R. = 0.7) $CH_4$/air flame at 0.1 and 0.9 MPa. *Overall parameter OP = $[\int \phi_L(\nu) \cdot \phi_{OH}(\nu) \cdot d\nu \cdot \eta_f \cdot F_B(J'', \upsilon'', T)]$

Fig. 2 OH molar fraction (*left-hand side scale*) simulated by OPPDIF and quenching rate ($s^{-1}$) profiles (*right-hand side scale*) calculated by the three models for a lean $CH_4$/air flame (E.R. = 0.7) at 0.1 and 0.9 MPa as a function of the distance from the bottom burner (in cm)

As the results between the different models are close, the following works will be performed using the Paul method, and as to our knowledge, it is known as the most recent model published in literature.

### 2.2.3 Boltzmann fraction calculation

For a given transition, the Boltzmann fraction $F_B$ depends on the temperature. So, it is helpful to select the laser pumped rotational level of the $X^2\Pi \; \upsilon'' = 0$ band in such a way that the Boltzmann fraction presents weak variations through the temperature domain where OH exists in a flame. In the present case, the Boltzmann fraction was calculated using spectroscopic constants taken from [31]. The temperature profile was simulated by the OPPDIF code [21], with the GRI-Mech 3.0 mechanism [22], for adiabatic flames.

## 2.3 Influence of the overall parameter (OP) variation on the fluorescence signal

In order to evaluate the influence of the overall parameter OP (that is the product of the spectral overlap, the quantum yield and the Boltzmann fraction) on the fluorescence signal profile, we compare both relative spatial profiles of the OH density population $N_{OH}$, calculated by the OPPDIF code [21] in conjunction with the GRI-Mech 3.0 mechanism [22] with $N_{OH}$ multiplied by OP, that represents an image of $S_f/E_L$; see Eq. (5).

Considering the different calculation methods presented above, the results are presented in Fig. 3 for lean $CH_4$/air (E.R. = 0.7) flames at 0.1 and 0.9 MPa. It clearly shows that the influence of the overall parameter variations on the fluorescence signal along the flame axis is very weak. This result is explained by the fact that the variation of the three parameters occurs in the flame fronts, where OH concentration gradients are very important.

Consequently, at a given pressure, the fluorescence signal profile reproduces accurately the $N_{OH}$ population density profile. Those observations lead to the conclusion that, in our conditions, the overall influence of the spectral overlap, quantum yield and Boltzmann fraction variations can be neglected across the flame.

Hence, the first scenario, as depicted in Sect. 2.2, applies and, in order to get absolute concentration of OH, a calibration measurement of the fluorescence signal in only one

point in the burned gases is sufficient. However, such calibration needs to be done for each flame condition. In the present work, this calibration phase was done through laser absorption spectroscopy coupled with Planar Laser Induced Fluorescence (PLIF).

Furthermore, according to Eq. (5), the variation of OP versus the total pressure should follow the same variation as $(S_F/E_L)/N_{OH}$. This will be further analyzed in Sect. 5.3 to assess the physical meaning of this important parameter.

## 3 Calibration technique

The experimental calibration technique selected here is laser absorption spectroscopy along the diameter of the flame. As it has been shown, in our conditions, the overall parameter variations are negligible across the flames. Thus, according to Eq. (5), the absolute $N_{OH}$ measurement in the burned gases becomes a reference point for the fluorescence signal measurements obtained across the flame and the spatial $N_{OH}$ profile can be deduced.

The concentration is determined through the measurements of the incident and of the transmitted laser intensities across the flame, $I_0(\nu)$ and $I(\nu)$ ($W\,m^2\,s^{-1}$) respectively, with the help of the Beer–Lambert's law. When the laser wavelength is tuned across an absorption line, the resulting measured line is the convolution product of the laser line with the absorption line. In the case where the laser line width is much narrower than the absorption line, such as in our conditions, the Beer–Lambert's law can be expressed as follows:

$$\int \ln\left(\frac{I(\nu)}{I_0(\nu)}\right) \cdot d\nu$$
$$= -B_{J''J'} \cdot \frac{h\nu}{c} \cdot l \cdot F_B(J'', \upsilon'') \cdot N_{OH} \qquad (7)$$

where $B_{J''J'}$ is the Einstein absorption coefficient ($m^3\,J^{-1}\,s^{-2}$) of the considered transition, $h$ is the Planck's constant (J s), $c$ is the speed of light ($m\,s^{-1}$), $l$ is the absorption length of the beam in the flame (m), and $F_B(J'', \upsilon'')$ is the Boltzmann's fraction related to the OH laser pumped level. The absorption length $l$ is experimentally determined through the use of Planar LIF on OH in each flame. This procedure is further explained in detail in Sect. 4.2.

## 4 Experimental set-up

### 4.1 Combustion facility

The high pressure facility (see Fig. 4) implemented at ICARE consists in a cylindrical stainless steel combustion chamber of 80 cm height and 25 cm diameter. This chamber is certified to withstand static pressures as high as 6.0 MPa
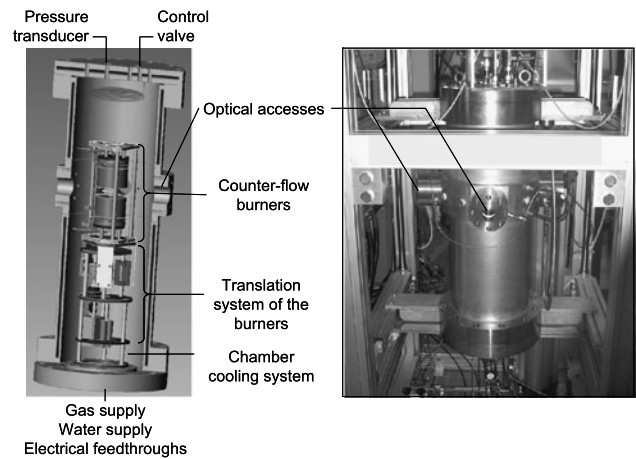
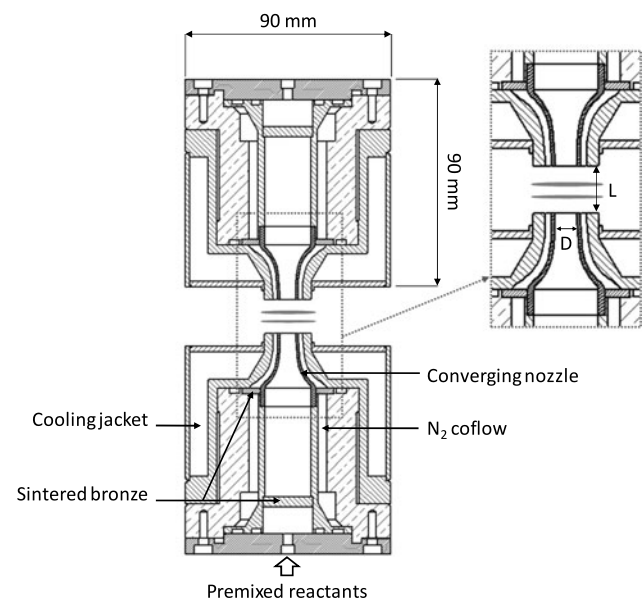**Fig. 4** Picture and diagram of the high pressure facility



**Fig. 5** Sketch of counterflow burner

and a maximum temperature at the inner wall of 200 °C. It is equipped with 4 opposite optical windows of 40 mm diameter dedicated to visualization and laser diagnostics. In order to avoid condensation on the windows, a weak flow of hot nitrogen is leaking the inner face of each window. The chamber is cooled with a water circulation in the doubled-wall cylinder and in the top cover.

The flames studied inside the chamber are stabilized between two twin counterflow burners (see Fig. 5). Each burner has an outer diameter of 90 mm and a height of 90 mm.

Each burner is composed of two coannular nozzles of 7 mm (D) and 13 mm diameter, which were aerodynamically shaped according to a modified empirical calculation from Rolon [32], resulting in a nearly uniform velocity profile on their exit, which enhances the flame stability

range [33]. The outer nozzle is used for a nitrogen coflow around the burner, which permits to isolate the flame from the surrounding gases. The distance between the nozzles of the burners (L) can be manually adjusted by moving the top burner compared with the bottom one. In the present study, the distance between the burners is fixed at 10 mm, leading to a L/D ratio equal to 1.4. Moreover, the lower burner can be laterally shifted in order to superimpose the axis of the burners. The burners are cooled using a closed loop water circulation at a fixed temperature between 30 and 45 °C, depending on the flame conditions, to avoid water condensation at the burners' surfaces.

Both burners are mounted on a vertical translation system located inside the chamber below the burners. This translation system is composed of a planetary roller screw (INA, RGTFS model) driven by a stepper motor (SEM, HDM58C6-73S model). Due to mechanical hysteresis, the precision of the positioning of the burners is about $\pm 50$ μm.

Gas flows (premixed gases and coflows), as well as cooling water and electrical wirings, are introduced through the bottom cover of the chamber. Burned gases are evacuated through the top cover. The pressure within the vessel is controlled with a pressure transducer (Wika, transmitter S-10 model) coupled with a control valve (Kämmer, 030037-IP model).

Different active and passive safety systems are installed in different places of the chamber. The passive ones include a safety valve (Swagelok, R4-C model) and a rupture disc (OSECO, FSTD model). The active ones include thermal (thermocouples J and K types) and pressure sensors which are connected to a programmable controller (Eurotherm, 2408 model). This latter controls different safety electro-pneumatic valves.

Gas flows are monitored with mass-flow controllers (Brooks, 5850S and 5850TR models), for each burner and for each gas, through a laboratory made Labview program. Each gas flow-meter is regularly and independently calibrated. Each gas line possesses a micrometric filter and a check valve installed upstream and downstream of the mass-flow controller, respectively. Gases of the premixture are mixed in a first cylindrical chamber filled with millimetric glass balls. A second downstream chamber serves as a buffer in order to attenuate the eventual flow fluctuations. Each of those chambers has an internal volume of 330 ml and can support 30 MPa.

For safety reasons, flames are ignited at atmospheric pressure with a retractable hot kanthal wire placed between the burners.

### 4.2 Laser diagnostic experimental set-up

#### 4.2.1 Laser induced fluorescence

The experimental set-up for LIF measurements is presented in Fig. 6. A tunable dye laser (Quanta-Ray, PDL-2) is
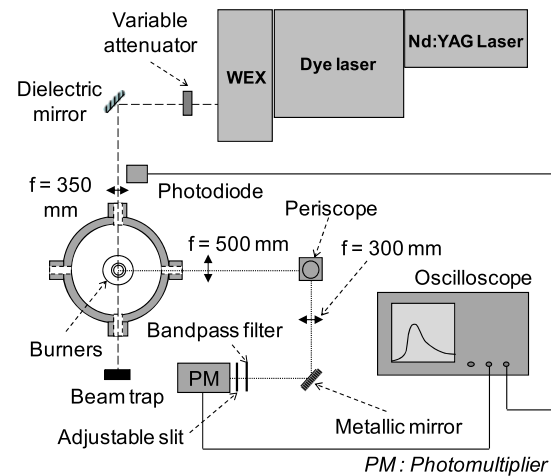


**Fig. 6** Experimental set-up diagram for the LIF measurements

pumped at 532 nm by a Nd:YAG pulsed laser (Quanta-Ray DCR-3), delivering 6 ns pulses at a repetition rate of 10 Hz. The laser beam of the dye laser is then doubled in frequency through a Wavelength EXpander (WEX) device. For fluorescence measurements, the dye used is Rhodamine 590, and the laser wavelength is tuned according to the $P_1(7)$ line of the $A^2\Sigma^+ - X^2\Pi$ (1, 0) band of OH at 285.00 nm. The choice of the $A - X$ (1, 0) band enables to limit laser absorption ahead of the probe volume (lower Franck–Condon factor than the $A - X$ (0, 0) band). The rotational level $N'' = 7$ is chosen as its Boltzmann fraction varies only slightly through the flame temperature domain (8 % between 1000 and 2000 K). The laser beam has a diameter of 6 mm, and delivers few milli-joules per pulse. The beam line shape is assumed to be Gaussian, with a linewidth of 0.1 cm$^{-1}$. In order to work on the linear regime of fluorescence of OH, the beam energy per pulse is reduced to less than 40 μJ with a variable attenuator composed of a half-wave plate and a Glan–Taylor prism. A part of the laser beam is collected by a fast photodiode (Newport, 818-BB-22 model) in order to monitor the laser beam energy fluctuations. The beam, which is vertically polarized, is then focused, with a $f = 350$ mm lens, inside the high pressure chamber, on the centre axis between the burners. Fluorescence signal is collected through a $f = 500$ mm lens and focused with a $f = 300$ mm lens on the entrance slit placed in front of a photomultiplier (PM) tube (Photonis XP2020Q). A 90° rotating periscope rotates the image of the probe volume and sets it parallel to the entrance slit. The entrance slit dimensions is 65 μm in width and 2.4 mm in height, giving a probe volume of 100 μm by 4 mm in the flame, according to the magnification ratio of the optical collection system. A LOT-Oriel bandpass filter ($\Delta\lambda = 25$ nm), centred at 313 nm, is installed at the entrance of the photomultiplier tube in order to collect the fluorescence signal of the OH $A^2\Sigma^+ - X^2\Pi$ (0, 0) and (1, 1) bands. Detected signals are

**Table 1** Experimental conditions of the counterflow CH$_4$/air premixed laminar flames with an equivalence ratio of E.R. = 0.7 and E.R. = 1

| | E.R. = 0.7 | | | | E.R. = 1 | |
|---|---|---|---|---|---|---|
| Pressure (MPa) | 0.1 | 0.3 | 0.5 | 0.7 | 0.1 | 0.3 |
| Laminar flame velocity (cm s$^{-1}$)[a] | 19.4 | 11.3 | 8.4 | 6.9 | 38.7 | 24.4 |
| Adiabatic flame temperature (K)[a] | 1818 | 1838 | 1837 | 1838 | 2140 | 2238 |
| Premixture flowrate (NL min$^{-1}$) | 1.57 | 2.51 | 2.98 | 4.01 | 2.75 | 7.56 |
| Premixture flow velocity (cm s$^{-1}$) | 76.3 | 42.0 | 30.9 | 29.7 | 133.9 | 126.8 |
| N$_2$ coflow velocity (cm s$^{-1}$) | 76.4 | 41.8 | 30.7 | 29.6 | 121.3 | 35.2 |

[a]Data calculated with PREMIX code [36] and GRI-Mech 3.0 mechanism [22]

finally sampled with a 1 GHz bandwidth oscilloscope (Tektronix, TDS5014B model).

### 4.2.2 Planar laser induced fluorescence

The excitation system of the PLIF measurements is very similar to the one used for LIF measurements. The $f = 350$ mm focusing lens is replaced by a $f = 500$ mm cylindrical lens, creating a laser sheet of 6 mm height and a thickness around 300 μm. The laser wavelength is tuned according to the P$_1$(7) line of the $A^2\Sigma^+ - X^2\Pi$ (1, 0) band of OH. Fluorescence is observed, at 90°, with an ICCD camera (Roper Scientific, PIMAX2), on which is mounted a UV lens (Nikkor, $f = 105$ mm) and 2 Schott filters (UG11 and WG295), allowing the collection of the fluorescence between 300 nm and 370 nm, in order to cover the $A^2\Sigma^+ - X^2\Pi$ (0, 0) and (1, 1) bands of OH. The gate width of the intensifier is fixed to 100 ns to limit flame emission disturbances. The CCD matrix of the camera is composed of a square 1024 × 1024 pixels of 13.1 μm edges. A spatial calibration of the images gives, considering a minimum of 2 adjacent pixels, a spatial resolution of 120 μm.

### 4.2.3 Laser absorption

Laser absorption spectroscopy measurements were performed according to the Q$_1$(8) line of the $A^2\Sigma^+ - X^2\Pi$ (0, 0) band ($\lambda = 309.24$ nm). To do so, the dye mixture of the laser was changed by a mixture of Sulforhodamine 640 and DCM diluted in methanol and ethanol, in order to be able to work on the $A^2\Sigma^+ - X^2\Pi$ (0, 0) band near 310 nm.

The beam size was reduced before the combustion chamber by a 200 μm aperture pinhole. The laser intensity signal with and without absorption ($I(\nu)$ and $I_0(\nu)$, respectively) were measured by a photodiode (2) placed behind the combustion chamber with and without flame, respectively. In order to take into account the pulse to pulse laser variations, a part of the laser beam was reflected toward a second identical photodiode (1) located upstream to the combustion chamber. Then the pulse to pulse laser intensity variation was taken into account by dividing the intensity measured by the photodiode (2) by the intensity measured by the photodiode (1). The OH concentration was measured in the burned
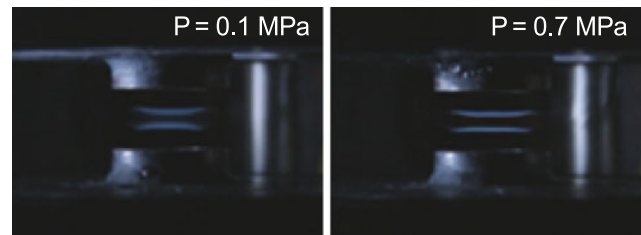


**Fig. 7** Pictures of the lean counterflow CH$_4$/air flames at 0.1 and 0.7 MPa

gases between the counterflow flames, where OH concentration gradients are weak, for each experimental condition.

## 5 Results and discussions

### 5.1 Flames conditions

In this paper, we present the experimental results for lean (E.R. = 0.7) and stoichiometric (E.R. = 1.0) CH$_4$/air flames at different pressures between 0.1 and 0.7 MPa. Experimental conditions of premixture flow and co-flow velocities at the exit of each burner are summarized in Table 1. Laminar flame velocities and adiabatic flame temperatures are also presented for each condition.

Pictures of lean CH$_4$/air flames at 0.1 and 0.7 MPa are presented in Fig. 7. Those pictures show that the flames are flat on a large area around the symmetric axis of the burners and are well pushed aside from the latter. Thus, heat exchanges between flames and the burners are quasinull and those stabilized counterflow flames can be considered as quasi-adiabatic.

### 5.2 Experimental data processing and results

#### 5.2.1 LIF

The fluorescence signal is measured at the temporal peak of fluorescence and the measurements are averaged on 200 laser pulses. LIF signal is then divided by the laser energy variations, measured by the photodiode (see Sect. 4.2.1), and corrected from the background signal. The latter is measured
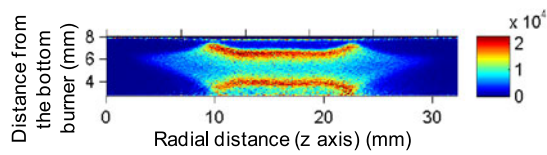
**Fig. 8** Example of a corrected PLIF image in the lean (E.R. = 0.7) CH$_4$/air flame at 0.3 MPa

by doing experiments in identical conditions with the laser tuned in a nonresonant wavelength. The optical system permits to realize LIF measurements with a spatial resolution of 100 µm in height and 4 mm in width.

The OH profile is measured two times for each flame and both profiles are averaged. This approach allows to check the good repeatability of the measurements and to verify the absence of problems during the experiment.

### 5.2.2 PLIF

In the same way as pointwise LIF experiments, care must be taken during the PLIF measurements in order to take into account the noise and the energy distribution along the laser sheet. Thus, for each flame, off-resonance fluorescence images were recorded as background images. The off-resonance image was subtracted from the raw image. In order to obtain a corrected fluorescence image representative of the OH concentration distribution in the flame, the vertical relative laser intensity distribution was measured by Rayleigh scattering from the same laser sheet. This experiment was made before each series of experiments, in the high pressure combustion chamber, without flame and filled with N$_2$ at 1 MPa. In this way, the corrected fluorescence signal was divided by the vertical laser energy distribution.

An example of results obtained by PLIF measurement is presented in Fig. 8 for the lean CH$_4$/air flame (E.R. = 0.7) at 0.3 MPa. One can notice that PLIF images validate the one-dimensional character of our flames along the symmetry axis of the counterflow burners.

The images are then post-processed using a homemade Matlab program, to extract the relative OH concentration radial profiles in the burned gases (i.e., between the flames). When we look at the radial profile (along the horizontal z-axis) of the fluorescence signal, it appears that it can be approximated by an isosceles trapezium (see Fig. 9) and its area $A_{\text{trapezium}}$ is given by the formula:

$$A_{\text{trapezium}} = \int_0^{L+2\ell} C(z)\,dz = (L+\ell)\cdot C_0 \tag{8}$$

where $C(z)$ is representative of the OH concentration as a function of the radial distance $z$, $C_0$ corresponds to the maximum OH concentration, and $L$ and $\ell$ are the radial length of the homogeneous and variable concentration zones of OH, respectively (see Fig. 9).
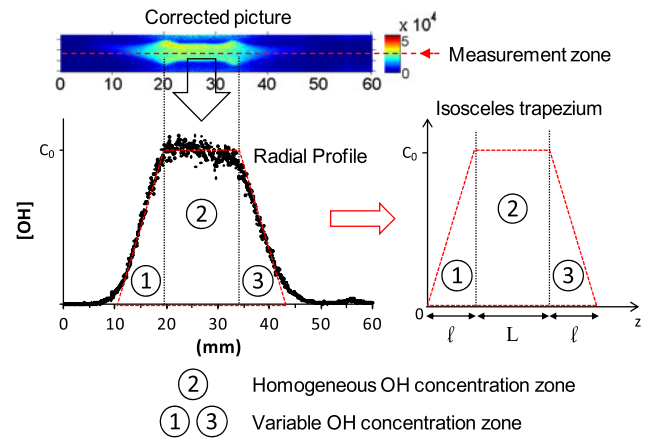


**Fig. 9** Example of the OH concentration distribution typically observed along the radial axis of a CH$_4$/air counterflow flame and comparison with an isosceles trapezium

**Table 2** Absorption path lengths (in mm) measured by PLIF in the burned gases of the counterflow CH$_4$/air flames for different equivalence ratios (E.R. = 0.7 and E.R. = 1) and different pressures (P = 0.1 to 0.7 MPa)

| Pressure (MPa) | Absorption path length (mm) | |
|---|---|---|
| | E.R. = 0.7 | E.R. = 1 |
| 0.1 | 18.5 | 24.7 |
| 0.3 | 18.6 | 32.5 |
| 0.5 | 18.9 | – |
| 0.7 | 19.6 | – |

It can be demonstrated that the application of the Beer–Lambert's law through such a concentration profile is equivalent to the one through a uniform profile with an amplitude of $C_0$ and an effective path length $l$ corresponding to the full width at half maximum $C_0$ (FWHM) of the trapezium profile. The equivalent absorption path length can then be calculated from the following equation:

$$l = \frac{\int C(z)\,dz}{C_0} \tag{9}$$

The experimental results of absorption path lengths for each flame are presented in Table 2. It shows that absorption path lengths vary significantly according to the equivalence ratio. Indeed, the absorption path length is around 19 mm for the lean CH$_4$/air flames. It is equal to 24.7 mm at atmospheric pressure and reaches 32.5 mm at 0.3 MPa for stoichiometric flames. Uncertainties on the path length measurements are ±6 %.

### 5.2.3 Laser absorption

Once the absorption path length is known, the Beer–Lambert's law (Eq. (7)) can be applied in order to determine the $N_{\text{OH}}$ density population and, by the way, the

OH molar fraction $X(OH)$. To do this, the Einstein absorption coefficient ($B_{J''J'}$) is obtained in the LIFBASE database [34] and the Boltzmann fraction is calculated by means of spectroscopic data provided in the Lucht et al. report [31], by considering the adiabatic flame temperature calculated with PREMIX and the GRI-Mech 3.0 mechanism (see Table 1). The ratio $I(\nu)/I_0(\nu)$ is measured by the photodiodes with and without flame, respectively. Examples of the experimental term $\{-\ln[I(\nu)/I_0(\nu)]\}$ as a function of frequency are presented in Fig. 10 for the lean $CH_4$/air flames at 0.1 MPa and 0.7 MPa. The experimental ratio $\{-\ln[I(\nu)/I_0(\nu)]\}$ is fitted considering a Voigt profile and the integral $\int -\ln(\frac{I(\nu)}{I_0(\nu)}) \cdot d\nu$ is calculated by measuring the area under this profile using the Origin software. It can be noticed that, at high pressure, the line shape does not return to the baseline (see Fig. 10b). This is probably due to the

presence of the $Q_{21}(8)$ line located just beside the $Q_1(8)$ line and to the increasing collisional broadening with pressure. This feature is a source of uncertainty and that is why the global uncertainties of $X(OH)$ measured in the burned gases are significantly higher at high pressure than at atmospheric pressure (31 % against 25 %). OH molar fractions measured in the burned gases of each flame by laser absorption are presented in Table 3.

### 5.2.4 Uncertainties

The equivalence ratios of the $CH_4$/air flames are $0.700 \pm 0.032$ and $1.000 \pm 0.032$. The absolute uncertainty on equivalence ratio was determined by a careful calibration of each flow-meter realized in our laboratory. The total uncertainty of the probe volume position is estimated at $\pm 100$ μm and increases at $\pm 170$ μm in the flame front due to deflection effects. The deflection of the laser beam was observed and measured on a screen 2 meters downstream the burners.

The uncertainty of the OH population density is estimated to be $\pm 19$ % at atmospheric pressure and $\pm 25$ % at high pressure. It takes into account the uncertainties of LIF measurements ($\pm 8$ %), path length ($\pm 6$ %), and integrated absorption line area ($\pm 3$ % at 0.1 MPa and $\pm 9$ % at higher pressure) and of the Boltzmann fraction ($\pm 2$ %) calculation.

$X(OH)$ is calculated using the perfect gas law assuming that the flame is adiabatic and determining adiabatic flame temperature through OPPDIF calculations [21] (GRI-Mech 3.0 mechanism [22]). The uncertainty on the calculated temperature is estimated to be around $\pm 5$ % and the uncertainty on pressure inside the combustion chamber is $\pm 1$ %. Consequently, the uncertainty of $X(OH)$ reaches $\pm 25$ % at atmospheric pressure and $\pm 31$ % at higher pressure.

### 5.3 OH molar fraction profiles and comparison with literature
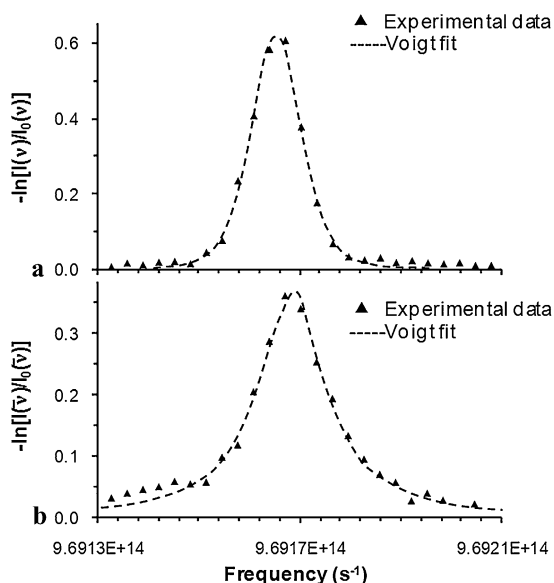


**Fig. 10** $\{-\ln[I(\nu)/I_0(\nu)]\}$ versus frequency (in $s^{-1}$) measured in the burned gases of the lean $CH_4$/air flame (E.R. = 0.7) at (**a**) 0.1 MPa and (**b**) 0.7 MPa. *Symbols*: experimental data, *dashed line*: fit with a Voigt profile

The OH molar fraction $X(OH)$ profiles measured in lean (E.R. = 0.7) and stoichiometric $CH_4$/air counterflow flames

**Table 3** OH molar fraction measured by laser absorption in the burned gases of the counterflow lean and stoichiometric $CH_4$/air flames, using four different methods (this work and methods A, B, and C)

A parameter $a$ calculated with $a = 450 P/T$ (Cattolica)
B parameter $a$ calculated with $a = 600 P/T$ (Lucht)
C parameter $a$ calculated with: $a = \sqrt{\ln 2}(\frac{\Delta \bar{\nu}_C}{\Delta \bar{\nu}_D})$

| | | Pressure (MPa) | | | |
|---|---|---|---|---|---|
| | | 0.1 | 0.3 | 0.5 | 0.7 |
| E.R. = 0.7 | This work | **2.91E–03** | **1.07E–03** | **5.14E–04** | **4.11E–04** |
| | A | 3.65E–03 | 1.32E–03 | 5.10E–04 | 4.01E–04 |
| | B | 3.58E–03 | 1.25E–03 | 4.90E–04 | 3.93E–04 |
| | C | 3.88E–03 | 1.35E–03 | 5.15E–04 | 4.05E–04 |
| E.R. = 1.0 | This work | **4.01E–03** | **2.17E–03** | – | – |
| | A | 6.41E–03 | 2.92E–03 | – | – |
| | B | 5.52E–03 | 2.56E–03 | – | – |
| | C | 6.74E–03 | 3.23E–03 | | |
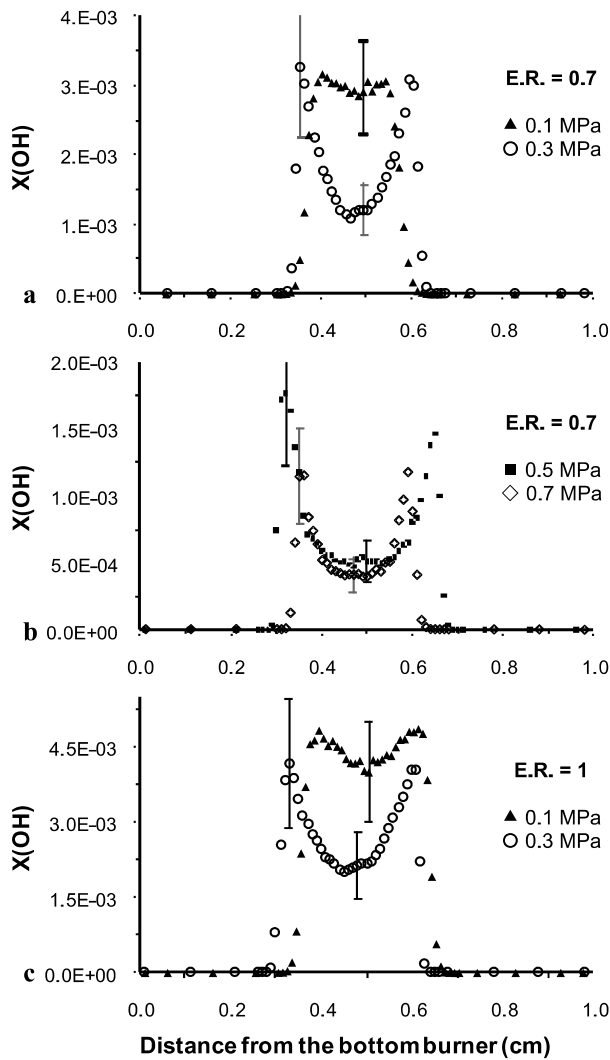
**Fig. 11** $X$(OH) profiles measured in the lean and stoichiometric counterflow $CH_4$/air flames at different pressures. (**a**) Equivalence ratio E.R. = 0.7 at 0.1 and 0.3 MPa; (**b**) Equivalence ratio E.R. = 0.7 at 0.5 and 0.7 MPa; (**c**) Equivalence ratio E.R. = 1.0 at 0.1 and 0.3 MPa

are presented in Fig. 11. The evolution of OH concentration through the flames is characterized by important gradients located in the flame fronts and a slight decrease in the burned gases at atmospheric pressure. The gradients of OH density in the burned gases, corresponding to the consuming phase of OH, are more marked in high pressure flames. This is due to the highest reactivity, linked to highest density and highest collision frequency, at high pressure.

OH molar fraction measurements in our counterflow flames were compared with literature data [8, 14, 39, 40] (see Table 4). Unfortunately, to our knowledge, absolute OH molar fraction profiles measurements in premixed counterflow flames at pressures above or equal to atmospheric pressure have not been published. Consequently, we focused on experiments realized on flat flame burners. It must be noted that counterflow flames and flat flames experiments cannot be compared directly. Indeed, it is well known that flames stabilized on flat flame burner are not adiabatic, because flame stabilization implies heat exchanges between the flame and the burner. Moreover, $X$(OH) decreases in the burned gases and consequently, a direct comparison of $X$(OH) in the burned gases of both types of flames is not immediate. Thus, we chose to compare our results to the range of $X$(OH) experimentally measured (minimum and maximum values) in the burned gases of flat flames (see Table 4, scheme b)).

The comparison shows that, according to the location where $X$(OH) is measured, similar values of $X$(OH) are obtained when comparing our results with data from the literature. Thus, it can be concluded that our measurement methodology is reliable. Considering the relatively low obtained uncertainties (detailed in Sect. 5.2.4) in our conditions, the present results demonstrate the capacity of the experimental set-up to allow the study of flame structure at high pressure.

For comparison, the method employed by Cattolica [35] and Lucht et al. [31] was also used to determine the OH concentration from our laser absorption measurements. This method, explained in detail in [35], consists in measuring the

**Table 4** (**a**) Comparison between $X$(OH) measurements data in the burned gases of $CH_4$/air flat flames from the literature [8, 14, 39, 40] and counterflow flames of this work. (**b**) Scheme of a typical $X$(OH) profile obtained in a flat flame

(a)

| E.R. | P (MPa) | | Desgroux et al. [14] | Domingues et al. [39] | Arnold et al. [8] | Biet et al. [40] | This work |
|---|---|---|---|---|---|---|---|
| 0.7 | 0.1 | min | – | – | – | 2.00E–03 | **2.91E–03** |
| | | max | – | – | – | 3.20E–03 | |
| 1 | 0.1 | min | 2.04E–03 | 2.16E–03[a] | 2.68E–03 | – | **4.01E–03** |
| | | max | 3.72E–03 | | 5.5E–03 | – | |
| | 0.3 | min | 7.46E–04 | – | – | – | **2.17E–03** |
| | | max | 1.65E–03 | – | – | – | |

(b)



[a]Measurements realized at 5 mm above the burner surface
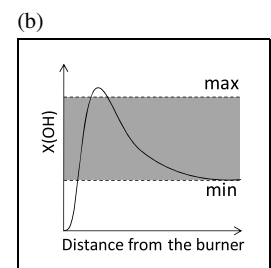
integrated absorption and calculating the broadening parameter $a$, defined by the theoretical formula: $a = \sqrt{\ln 2} \cdot \left(\frac{\Delta\bar{\nu}_C}{\Delta\bar{\nu}_D}\right)$ where $\Delta\bar{\nu}_C$ and $\Delta\bar{\nu}_D$ are the Lorentzian (collisional) and Gaussian (Doppler) widths of the Voigt absorption line shape, respectively. The absorption coefficient is calculated from tabulated curves of growth, presented in [31], and the OH concentration is deduced.

Cattolica [35] and Lucht et al. [31] both used a simplified formulation of the $a$ parameter, considering a transition in the $A - X$ $(0,0)$ vibrational band:

$$a = C \cdot \left(\frac{P}{T}\right) \tag{10}$$

where $C$ is an experimentally determined constant, $P$ the pressure (atm) and $T$ the temperature (K).

Cattolica used a constant $C = 450$ for OH, according to the work of Nadler and Kaskan [37], which considered only the $P_1(5)$ line of the $A - X$ $(0,0)$ band. Lucht proposed a constant $C = 600$ by averaging results of Nadler and Kaskan [37] and Engelman [38] over more rotational numbers. From our experimental absorption measurements, we propose here to deduce the OH concentration using the curves of growth from [31] and the different values of $a$ according to the three following methods:

Method A (Cattolica): $a = 450\ P/T$
Method B (Lucht et al.): $a = 600\ P/T$
Method C: $a = \sqrt{\ln 2} \cdot \left(\frac{\Delta\bar{\nu}_C}{\Delta\bar{\nu}_D}\right)$

In the last case, $\Delta\bar{\nu}_C$ and $\Delta\bar{\nu}_D$ were calculated using methods described in Sect. 2.2.1.

The results, presented in Table 3, show differences according to the method employed, especially at atmospheric pressure for both equivalence ratios. The differences between results obtained from our method and results using the method of Cattolica ($a = 450\ P/T$) can reach 25 % for the lean flame and as much as 60 % for the stoichiometric one. At higher pressures, the differences decrease and results obtained with the four methods are very close to each other. In all cases, the method of Lucht et al. with $a = 600\ P/T$ gives the best agreement with our method.

Important uncertainties are associated to the calculation of the parameter $a$. As shown in Fig. 1 of [35], which represents the curve of growth as a function of the parameter $a$:

- if the value of $a$ is high and the integrated absorption is relatively low, which is our case at high pressure, the accuracy with which $a$ is calculated will have weak influence on the determination of the absorption coefficient.
- however, if the value of $a$ is lower and the integrated absorption is higher, which is our case at atmospheric pressure, this will have a great influence on the OH concentration determination.

This explains the differences observed between the four methods (A, B, and C and the Beer–Lambert's methods) in
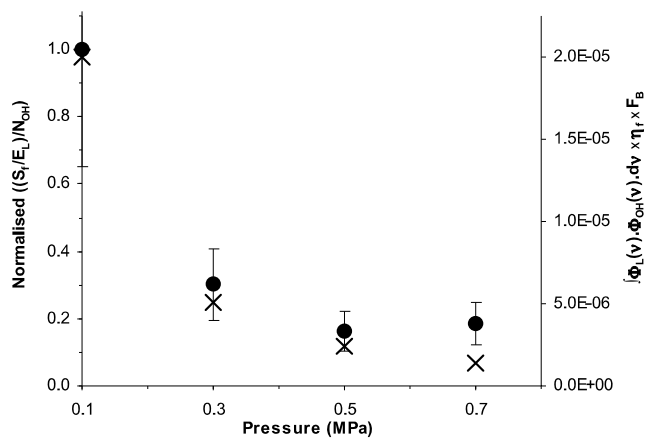


**Fig. 12** Comparison between the normalized ratio of experimental fluorescence signal on OH population density: $[(S_f/E_L)/N_{OH}]$ (symbol: $\bullet$, *left-hand scale*) measured in the burned gases of the lean CH$_4$/air flame and the overall parameter OP (symbol: $\times$, *right-hand scale*) at different pressures (0.1 to 0.7 MPa)

our atmospheric pressure flames. However, at higher pressure, the influence of the parameter $a$ becomes nearly negligible, and results are closer to each other.

Based on these observations, one can conclude that the Cattolica's method seems to be less adapted to $X$(OH) measurement when absorption is important, due to the high uncertainties linked to the calculation of the parameter $a$. In this case, our method gives more accurate results, as long as the laser line shape is narrow compared to the absorption line.

As mentioned at the end of Sect. 2.2.3, once the absolute concentration of OH is determined, the validity of the overall parameter OP evaluation can be checked. On that purpose, based on relation (5), we compared the relative behaviour versus pressure of the experimentally determined term $(S_f/E_L)/N_{OH}$ with the one of the calculated overall parameter. Calculations and experimental values, presented in Fig. 12, are given for the burned gases of lean (E.R. = 0.7) CH$_4$/air flames at 0.1 to 0.7 MPa. The results show that the overall parameter decreases as the pressure increases according to a function close to $1/P$. This behavior is due to the fact that the quantum yield variations are dominant. The comparison between experimental and calculated data shows that, taking into account uncertainties linked to calculations and experimental measurements, the agreement is fairly good. Hence, our evaluation of the overall parameter, in the studied range of pressure, has a realistic coherence.

To conclude, the methodology employed in this work, i.e., a combination of three diagnostic techniques (LIF, PLIF, and Absorption) with careful calculations or evaluations of spectroscopic parameters that could influence the OH measured signal, is validated in our high pressure counterflow flames conditions. This gives confidence for future species profiles measurements by laser techniques in our system.

## 6 Conclusions

The aim of the present work was to validate the ability of the new experimental device implemented at the ICARE laboratory to allow the achievement of high pressure premixed flame structure studies. To do this, OH molar fraction profiles have been measured in $CH_4$/air counterflow flames until 0.7 MPa thanks to the combination of three optical diagnostic methods: LIF, PLIF, and laser absorption. High pressure LIF measurements are greatly complicated by the variations of pressure and temperature dependant parameters which locally modify the ratio between fluorescence signal and OH concentration. Consequently, an important work has been devoted to the evaluation of the influence of those parameters on the fluorescence signal. This study led to the conclusion that, for our conditions, these variations could be neglected, at a given pressure, across the flame. Thus, careful individual calibration of the fluorescence signal in each flame permits to avoid the laborious and complicated calculations of the aforementioned parameters. Calibration has been realized by leaning on PLIF measurements, to accurately determine the absorption path-length, and by using Beer–Lambert's law for absorption measurements. $X(OH)$ molar fractions measured in the burned gases of our flames were compared with literature data. A good coherence between results has been observed.

The good quality of the results demonstrates the capacity of the system for species profiles measurements in high pressure premixed flames. The second step of this study is to compare experimental results to the modeling in order to assess the ability of kinetic mechanisms to accurately reproduce $X(OH)$ experimental profiles in high pressure flames. This topic will be dealt with in a future paper.

## References

1. C. Vovelle, J.-L. Delfau, L. Pillier, Combust. Explos. Shock Waves **45**, 365 (2009)
2. K. Kohse-Höinghaus, A. Brockhinke, Combust. Explos. Shock Waves **45**, 349 (2009)
3. K. Kohse-Höinghaus, Prog. Energy Combust. Sci. **20**, 203 (1994)
4. G. Singla, P. Scouflaire, C. Rolon, S. Candel, Combust. Flame **144**, 151 (2006)
5. M.G. Allen, K.R. McManus, D.M. Sonnenfroh, P.H. Paul, Appl. Opt. **34**, 6287 (1995)
6. W.G. Bessler, C. Schulz, T. Lee, J.B. Jeffries, R.K. Hanson, Appl. Opt. **41**, 3547 (2002)
7. B.E. Battles, R.K. Hanson, J. Quant. Spectrosc. Radiat. Transf. **54**, 521 (1995)
8. A. Arnold, R. Bombach, B. Käppeli, A. Schlegel, Appl. Phys. B **64**, 579 (1997)
9. Q.V. Nguyen, R.W. Dibble, C.D. Carter, G.J. Fiechtner, R.S. Barlow, Combust. Flame **105**, 499 (1996)
10. B. Atakan, J. Heinze, U.E. Meier, Appl. Phys. B **64**, 585 (1997)
11. J.E. Siow, N.M. Laurendeau, Combust. Flame **136**, 16 (2004)
12. R.V. Ravikrishna, N.M. Laurendeau, Proc. Inst. Mech. Eng., A J. Power Energy **217**, 529 (2003)
13. C.D. Carter, J.T. Salmon, G.B. King, N.M. Laurendeau, Appl. Opt. **26**, 4551 (1987)
14. P. Desgroux, E. Domingues, M.-J. Cottereau, Appl. Opt. **31**, 2831 (1992)
15. C.D. Carter, N.M. Laurendeau, Appl. Phys. B **58**, 519 (1994)
16. P. Andresen, H. Schlüter, D. Wolff, H. Voges, A. Koch, W. Hentschel, W. Oppermann, E. Rothe, Appl. Opt. **31**, 7684 (1992)
17. M. Mansour, Y.-C. Chen, Exp. Therm. Fluid Sci. **32**, 1390 (2008)
18. A.A. Konnov, M. Idir, J.-L. Delfau, C. Vovelle, Combust. Flame **105**, 308 (1996)
19. A. Fayoux, K. Zähringer, O. Gicquel, J.C. Rolon, Proc. Combust. Inst. **30**, 251 (2005)
20. J.-I. Kim, J.Y. Hwang, J. Lee, M. Choi, S.H. Chung, Int. J. Heat Mass Transf. **48**, 75 (2005)
21. A.E. Lutz, R.J. Kee, J.F. Grcar, F.M. Rupley, Sandia National Laboratory report N° SAND96-8243 (1997)
22. G.P. Smith, D.M. Golden, M. Frenklach, N.W. Moriarty, B. Eiteneer, M. Goldenberg, C.T. Bowman, R.K. Hanson, S. Song, W.C. Gardiner et al., GRImech3.0 mechanism (1999). http://www.me.berkeley.edu/gri_mech/
23. E.C. Rea, A.Y. Chang, R.K. Hanson, J. Quant. Spectrosc. Radiat. Transf. **41**, 29 (1989)
24. S.M. Hwang, J.N. Kojima, Q.-V. Nguyen, M.J. Rabinowitz, J. Quant. Spectrosc. Radiat. Transf. **109**, 2715 (2008)
25. A. Bresson, Ph.D. thesis, Université de Rouen, France (2000)
26. A. Bülter, U. Lenhard, U. Rahmann, K. Kohse-Höinghaus, B. Andreas, in *LASKIN, Laser Applications to Chemical and Environmental Analysis (LACEA)*, Annapolis, Maryland (Etats-Unis) (2004)
27. R. Schwarzwald, P. Monkhouse, J. Wolfrum, Chem. Phys. Lett. **142**, 15 (1987)
28. M. Tsujishita, A. Hirano, Appl. Phys. B, Lasers Opt. **62**, 255 (1996)
29. N.L. Garland, D.R. Crosley, Proc. Combust. Inst. **21**, 1693 (1986)
30. P.H. Paul, J. Quant. Spectrosc. Radiat. Transf. **51**, 511 (1994)
31. R.P. Lucht, R.C. Peterson, N.M. Laurendeau, Purdue University report N° PURDU-CL-78-06 (1978)
32. J.C. Rolon, Ph.D. thesis, Ecole Centrale Paris, France (1988)
33. N. Bouvet, Ph.D. thesis, Université d'Orléans, France (2009)
34. J. Luque, D.R. Crosley, LIFBASE, SRI International Report MP 99-009 (1999)
35. R.J. Cattolica, Sandia National Laboratory report N° SAND79-8717 (1979)
36. R.J. Kee, J.F. Grcar, M.D. Smooke, J.A. Miller, PREMIX, Sandia National Laboratory Report SAND85-8240 (1985)
37. M. Nadler, W.E. Kaskan, J. Quant. Spectrosc. Radiat. Transf. **10**, 25 (1970)
38. R. Engleman, J. Quant. Spectrosc. Radiat. Transf. **9**, 391 (1969)
39. E. Domingues, M.-J. Cottereau, D.A. Feikema, Int. J. Energ. Mater. Chem. Propuls. **3**, 167 (1994)
40. J. Biet, J.-L. Delfau, L. Pillier, C. Vovelle, in *Proc. of the European Combustion Meeting*, Chania, Greece, 11–13 April (2007)